physica status solidi

pss

www.pss-journals.com

reprint

WILEY-VCH

Phys. Status Solidi B **249,** No. 9, 1709–1716 (2012) / **DOI** 10.1002/pssb.201248193

physica status solidi b
www.pss-b.com
basic solid state physics

Kinetic Monte Carlo approach for triangular-shaped Pt islands on Pt(111) surfaces

Robert Deák[1,2] **and Zoltán Néda**[*,1]

[1] Department of Theoretical Physics, Babeş-Bolyai University, 400084 Cluj-Napoca, Romania
[2] Department of Materials Physics, Eötvös Loránd University, 1117 Budapest, Hungary

Received 20 February 2012, revised 18 April 2012, accepted 27 April 2012
Published online 4 June 2012

Keywords kinetic Monte Carlo, nanoscale islands, pattern formation on surfaces, surface diffusion

[*] Corresponding author: e-mail zneda@phys.ubbcluj.ro, Phone: +40 264 405300, Fax: +40 264 591906

Formation of triangular-shaped Pt adatom islands on a Pt(111) surface is investigated using a kinetic Monte Carlo approach. The energy barriers are calculated with the generalized embedded atom method and the nudged elastic band approach. The numerical results reveal that the preferential orientation of the triangles cannot be explained solely by the differences in the diffusion coefficients of the atoms along the topologically non-equivalent edges of the islands. For a self-consistent explanation of the triangle orientations, one has to examine the topological and energetic details of the diffusion paths for all the edge diffusion processes, kink-formation or kink-breaking events, and corner to edge jumps.

1 Introduction In the last two decades, several experimental and theoretical studies were carried out in order to understand the morphology of two-dimensional (2D) islands formed by atoms deposited on crystalline surfaces [1–11]. Besides the obvious interest from the view of basic solid-state physics, such island morphologies might also be important for engineering various nanostructures with practical interest: nanodots, photonic crystals, or patterned surfaces [12]. In the present work we will study the topological and energetic details for the formation of compact islands on the (111) surface of face centered cubic (FCC) metals. On such surfaces the islands are bounded by two types of topologically non-equivalent steps (edges). These are the (100) microfacet (type A) and the (111) microfacet (type B), as can be seen in Fig. 1.

During epitaxial deposition of Pt on the Pt(111) surface in a quite broad temperature and deposition flux range, triangular-shaped 2D adatom islands are formed. As a function of the type of the triangle edges, these islands can be of A- or B-type (see Fig. 2). Usually at a parameter set just one type of triangular islands can be observed.

Michely et al. [1] reported an interesting inversion of the triangle orientation as the temperature of the sample was changed. The experiments were performed in a special scanning tunneling microscope (STM) apparatus where the temperature could be controlled in a quite broad interval. At low temperatures the nucleated atoms formed islands of fractal or dendritic shape and at higher temperatures the islands became compact. It has been found that by increasing the substrate temperature the compact island can select triangular (bounded by A steps), hexagonal (bounded by A and B steps), inverted triangular (bounded by B steps), and again hexagonal shape. Based on earlier studies for the temperature dependence of the diffusion coefficient on the A-type and B-type channels [13], the triangular shape of the islands was attributed to the difference in the diffusion speeds of the adatoms along the A- and B-type steps. It was assumed that the lower the adatom migration speed along a step edge, the higher the probability of a new step nucleation. Therefore, the advancement of this step is faster and as a result of this the step will disappear more quickly in time. For lower temperatures, where the triangular shape on A-type edges is dominating, Michely et al. concluded that the diffusion coefficient along the A steps (D_A) should be larger than the one along the B steps (D_B). For higher temperatures the opposite should be true and for temperatures where the island has hexagonal shape, naturally $D_A \approx D_B$ was assumed. No microscopic mechanism supporting these assumptions was given, however.

The same group who reported the experimental study about the temperature-dependent shape change of the Pt islands published in 1998 an interesting new result [2]. They revealed that the triangle orientation at low temperatures is an effect of carbon monoxide (CO) impurities which are

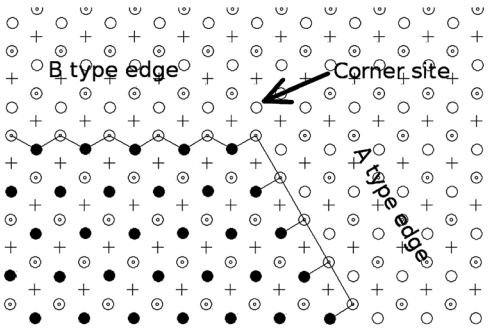

Figure 1 Geometry of the *A*- and *B*-type edges. Dotted circles represent the sites of the substrate, circles and crosses represent the FCC and HCP lattice sites of the growing layer, respectively. The filled circles are the FCC sites of the growing layer which are already occupied by the adatoms.

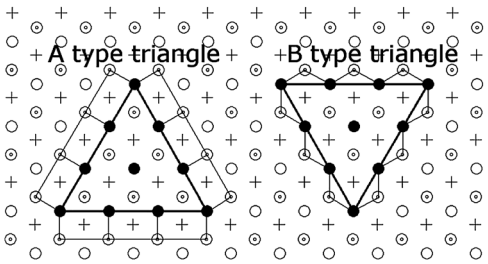

Figure 2 Topology of small *A*- and *B*-type triangular FCC islands, bounded, respectively, by only *A*- and *B*-type edges. Dotted circles represent the sites of the substrate, circles and crosses represent the FCC and HCP lattice sites of the growing layer, respectively. The filled circles are the occupied FCC sites of the growing layer.

sticking preferentially to *A* steps. By reducing the amount of CO in the deposition chamber, only islands bounded to *B* steps are observed at any temperature. Therefore, the inversion of the triangle orientation is not a purely temperature effect, as was assumed earlier. Seemingly at low temperatures CO passivates the *A*-step atoms more efficiently than those on the *B* steps, leading to higher diffusion on *A* steps, and as a consequence of this a faster advancement and disappearance of *B* steps. At high temperatures the lifetime of CO bounded to the Pt(111) surface is small, and thus the normal orientation of triangles (bounded to *B* steps) is observed. The formation of the triangular-shaped islands bounded at the *B* step was assumed to be similar to the case of Ir [14], where the responsible phenomenon is the net flux of adatoms from *B* steps to *A* steps.

Over the years several theoretical studies were done to explore the atomistic mechanism for the shape selection and orientation of the Pt islands on Pt(111) surfaces. By rescaling the theoretically calculated energy barrier values for different elementary FCC–FCC atomic movements [15], or by choosing the hopping energies in a consistent manner with the field ion microscope (FIM) experimentally measured values [16], kinetic Monte Carlo (kMC) simulations were able to find parameter sets that reproduced the experimentally observed compact island shapes and the transitions between them.

Theoretical explanations were pointing not only to the discussed edge diffusion anisotropy, but considered also the kink-breaking and corner-crossing phenomena. For the dendritic Ag or Pt islands (with a triangular envelope) formed on the Pt(111) surface, Brune [5] and Brune et al. [6] found by effective medium theory (EMT) calculations that the responsible processes are the anisotropic jumps from corners to different types of edges (*A* or *B*). A kMC study performed with first-principles parameters for compact Al islands on the Al(111) surface [7] showed that reversing the edge diffusion anisotropy has no effect on the orientation of the triangular islands. The island orientation changes only when the corner diffusion anisotropy is reversed. The same conclusion was derived also for compact Pt islands by Wu et al. [4]. This group used also kMC simulations to clarify the main mechanisms responsible for the formation of the triangular-shaped islands and the inversion of their orientation. In their study, three elementary atomic processes are discussed: (i) the edge diffusion, characterized by the activation energy $E_{2\to2}$; (ii) the edge to corner diffusion, with activation energy $E_{2\to1}$; and (iii) the corner to edge diffusion, with activation energy $E_{1\to2}$. Generally, one would expect for a given type of edge the following relation between these energies: $E_{1\to2} < E_{2\to2} < E_{2\to1}$. Using activation energies for Pt strictly from Feibelman's first-principles calculation [3] for a clean Pt epitaxial growth, they found islands bounded by *B*-steps only, independently of the surface temperature values. They also concluded that the only parameter that could influence the inversion of triangles is the edge to corner energy barrier. By interchanging their values for *A* and *B* steps, the triangular islands changed their orientation. It was thus assumed that the presence of CO will weaken the binding energy of Pt at the *A* step so much that the difference in the edge to corner diffusion rates for the two steps is reversed in sign. Arguments based on the energetics of the diffusing atoms are given also in the book of Michely and Krug [8] and in the seminal paper of Evans et al. [9]. Besides kMC simulation methods for investigating this problem, it is worth mentioning an approach based on genetic algorithms for optimizing the shape of 2D adatom islands on (111) surfaces [10] and a dynamical model based on surface interaction potentials and *ab initio* calculations [11].

In the present work we continue the investigations concerning the formation of the triangular-shaped compact Pt islands on Pt(111) surfaces, and give further details about its kinetics, using a previously tested lattice kMC method [19]. We feel that a numerical study based on the generalized embedded atom method (gEAM) and on the nudged elastic band (NEB) calculation method for the hopping energy barriers can still be useful for understanding this interesting phenomenon. The present paper is organized as follows. In

Section 2 we present briefly the used kMC method and its parameters. In Section 3 we present the obtained simulation results and discuss numerical calculations for the microscopic mechanisms responsible for the formation of triangular-shaped islands. Section 4 is devoted to our conclusions.

2 The used kMC method and computational details Lattice kMC methods proved to be appropriate for studying several phenomena related to the epitaxial growth of thin films, such as island nucleation, growth and coalescence [17], island diffusion [18, 19], stacking fault related phase boundary [20], and even co-deposition of several types of atoms [21, 20].

The kMC method is useful for simulating those dynamical phenomena where processes with widely different rates are simultaneously present. In the case of the epitaxial growth or surface diffusion this is the case: (i) atoms can be deposited on a crystalline surface with a given rate; (ii) atoms can diffuse on the surface governed by hopping rates that are determined by their interaction energy with neighboring atoms; (iii) decohesion of surface atoms can occur with a given rate. The main idea of the kMC simulation method [22] is that in each simulation step one process is randomly selected (with probability proportional with its rate) and carried out. The time is updated non-uniformly and non-deterministically, depending on the rates of all possible processes at that given moment [22]. For thin-film growth simulations generally, the *deposition rate* is fixed and calculated from the deposition speed (deposition flux) given as the number of new monolayers deposited in unit time (ml/s). The *diffusion rate* $(r_{X\to Y})$ of an atom is governed by the thermodynamic temperature (T) of the system and the potential barrier $(\Delta U_{X\to Y})$ that the atom has to overcome between the initial (X) and the final (Y) positions:

$$r_{X\to Y} = f_0 \exp\left(-\frac{\Delta U_{X\to Y}}{k_B T}\right). \tag{1}$$

In expression (1), k_B is the Boltzmann factor and f_0 is the attempt rate, which is roughly the vibration frequency of atoms in the crystal ($f_0 = 10^{12}$ Hz). Since the value of the barrier is not straightforward to estimate (even if the pair-interaction potential between the atoms is known), several approximating methods are used [23–26]. The *desorption rate* is obtained either by fixing a phenomenological potential barrier E_{dec} for this process or by calculating the more realistic potential barrier from first principles, as the binding energy of the chosen atom at the given site. Simulations are usually performed in a 2D geometry, the atoms being allowed to occupy the sites of a pre-defined lattice. By this approach one reproduces an idealized situation where a new layer is growing on a perfect crystalline substrate.

Here, the kMC method is used for modeling the formation of 2D triangular-shaped Pt adatom islands during the sub-monolayer epitaxial growth on a Pt(111) surface. The method was already tested and its applicability was proven in a recent study concerning the 2D self-diffusion of Pt atom clusters on a Pt(111) surface [19]. A bulk FCC substrate is considered with a (111) triangular lattice surface. The accepted 2.77×10^{-10} m lattice constant value is used for the surface atoms [19]. The atoms can be deposited and can diffuse on this surface using the sites of the two available sublattices, namely the FCC and hexagonal close packed (HCP) sites (Fig. 1). The interaction potentials between the atoms are calculated using the gEAM potential [27, 28]; the hopping barrier is determined by the NEB method [24, 25]. Similarly with our earlier study [19], only in-layer single-atom diffusion mechanisms are considered. Furthermore, for any non-zero deposition flux we consider that the atoms deposited on the top of an existing island are automatically reassigned for a randomly selected site on the edges of the island. This rearrangement does not alter the random site deposition in a sub-monolayer epitaxial growth process and speeds up the simulation by handling elegantly the diffusion of the atoms on the top of the islands and their final jumps to the island edges. Simulations are done with both zero and non-zero deposition fluxes.

2.1 Calculation of the hopping barrier The NEB method [24, 25] is used for finding the minimum energy path (MEP) of every atomic jump. This method is efficient in determining the saddle points, and therefore the energy barrier for transitions with given initial and final states. The method uses a number of replicas of the moving atom, displaced along a continuous path between the initial and final states of the transition. The replicas are connected with fictitious springs acting only along the path and ensuring its continuity. The external forces are projected however orthogonally to this path. The relaxing force acting on the ith image may be written as

$$\begin{aligned}\mathbf{F}_i^{\mathrm{rel}} &= -\nabla U(\mathbf{R}_i)|_{\perp} + (\mathbf{F}_i^{\mathrm{spring}} \cdot \boldsymbol{\tau}_i)\boldsymbol{\tau}_i \\ &= -\nabla U(\mathbf{R}_i) + [\nabla U(\mathbf{R}_i) \cdot \boldsymbol{\tau}_i]\boldsymbol{\tau}_i \\ &\quad + [k(\mathbf{R}_{i+1} + \mathbf{R}_{i-1} - 2\mathbf{R}_i) \cdot \boldsymbol{\tau}_i]\boldsymbol{\tau}_i,\end{aligned} \tag{2}$$

where k is the spring constant, $\boldsymbol{R}_i$ the coordinate vector of the ith image, $U(\boldsymbol{R}_i)$ the potential, and $\mathbf{F}_i^{\mathrm{spring}}$ is the spring force acting on the image. $\boldsymbol{\tau}_i$ is the normalized tangent vector at the location of the ith image, used to project the desired components of the forces. $\perp$ represents the perpendicular projections of the vectors relative to the tangent vector.

The initial coordinates of the replicas which are forming the band are determined by a simple linear interpolation between the initial and final states of the assumed jump. In order to reach the MEP, the band is optimized using the steepest descent method. The energy barrier of the transition is taken as the sum of the differences between the consecutive potential energy minima and maxima along the oriented MEP. Usually, multiple energy minima and maxima can appear on the MEP when the path passes in the neighborhood of an intermediate lattice site. Such situation

can appear for example in an FCC–FCC jump, where the path contains an intermediate minimum due to a neighboring HCP site. In the present work we consider the band discretized with 19 replicas and the used spring constant is chosen as $k = 0.65$ eV/Å.

2.2 Interatomic potential The gEAM potential [27, 28] was used to calculate the interatomic potentials. The gEAM potential is a many-body approach which was used with success for calculating bulk properties of multilayer films [28], but also successfully applied in kMC simulation for surface diffusion of 2D Pt islands on Pt(111) surfaces [19] and for molecular dynamics (MD) simulation for structural deformation and mechanical strength of a defective Cu nanowire, which contains about 22–38% surface atoms [29]. In the gEAM approach the potential energy for an atom i is the sum of two terms:

$$U_i = \sum_{j \neq i} \phi(r_{ij}) + F(\rho_i). \tag{3}$$

The first term contains the pair-interaction potentials between the ith and all the other atoms:

$$\phi(r_{ij}) = \frac{A \times \exp\left[-\alpha\left(\frac{r_{ij}}{r_e} - 1\right)\right]}{1 + \left(\frac{r_{ij}}{r_e} - \kappa\right)^{20}} - \frac{B \times \exp\left[-\beta\left(\frac{r_{ij}}{r_e} - 1\right)\right]}{1 + \left(\frac{r_{ij}}{r_e} - \lambda\right)^{20}}, \tag{4}$$

where r_{ij} is the distance between atoms i and j and r_e is the equilibrium distance between nearest-neighbor atoms. A, B, α, β, κ, and λ are adjustable parameters of the potential.

The second term of Eq. (3) is the many-body term resulting from the interaction energy which is needed to embed the ith atom in the local-electron density, ρ_i, provided by the other atoms. To ensure a well-working embedding energy function over a wide range of electron density, three cases are separated, $\rho_i < \rho_n$, $\rho_n \leq \rho_i < \rho_0$, and $\rho_0 \leq \rho_i$, where $\rho_n = 0.85\ \rho_e$, $\rho_0 = 1.15\rho_e$ and ρ_e is the equilibrium electron density:

$$F(\rho_i) = \begin{cases} \sum_{x=0}^{3} F_{nx}\left(\frac{\rho_i}{\rho_n} - 1\right)^x & \text{if } \rho_i < \rho_n, \rho_n = 0.85\rho_e, \\ \sum_{x=0}^{3} F_x\left(\frac{\rho_i}{\rho_n} - 1\right)^x & \text{if } \rho_n \leq \rho_i < \rho_0, \\ & \rho_0 = 1.15\rho_e, \\ F_e\left[1 - \ln\left(\frac{\rho_i}{\rho_e}\right)^\eta\right]\left(\frac{\rho_i}{\rho_e}\right)^\eta & \text{if } \rho_0 \leq \rho_i. \end{cases} \tag{5}$$

The local-electron density ρ_i can be calculated using

$$\rho_i = \sum_{j \neq i} f_j(r_{ij}), \tag{6}$$

where $f_j(r_{ij})$ is the electron density of atom i, which can be written as

$$f_j(r_{ij}) = \frac{f_e \times \exp\left[-\beta\left(\frac{r_{ij}}{r_e} - 1\right)\right]}{1 + \left(\frac{r_{ij}}{r_e} - \lambda\right)^{20}}, \tag{7}$$

where f_e is the equilibrium electron density.

All the parameters that are used in the above equations for the case of Pt are listed in Table 1.

It is known that gEAM is a less accurate approximation than the *ab initio* methods (for a review, see Ref. [30]). However, *ab initio* MD simulations need extremely long computational time and therefore the applications of such potentials are restricted for relatively small systems and short simulation times. For simulating a surface phenomenon with a longer time evolution (seconds or minutes), a list of hopping barriers of pre-defined events is used from *ab initio* calculations [4, 7]. Another possibility is to use rescaled theoretical [15] or experimental [16] barrier values or to use semi-empirical potentials [28]. Here, in order to maintain a reasonable speed and accuracy we use lattice kMC simulations, the gEAM method to calculate the potential and the NEB method with 19 replicas to calculate the MEP and the hopping barrier of all possible diffusion jumps. By using this method we take into account also the complete surroundings of the jumping atoms over the paths, leading to more realistic effective potential barrier values. Since gEAM is mainly used for bulk systems, its use for surface diffusion processes on Pt(111) surfaces can be debated. However, in a previous study [19] we have shown that it predicts proper migration energy values for the diffusion of free atoms on surfaces. For the free diffusion of one Pt atom on a Pt(111) surface, the method predicts an effective migration barrier energy $E_m = 0.2$ eV. This is in acceptable agreement with the $E_m = 0.26 \pm 0.03$ eV results indicated by FIM experiments

Table 1 gEAM parameters for Pt.

r_e (Å)	2.771
f_e (eV/Å)	2.336
ρ_e (eV/Å)	34.108
α	7.079
β	3.775
A (eV)	0.449
B (eV)	0.593
κ	0.413
λ	0.826
η	1.393
F_{n0} (eV)	−4.099
F_{n1} (eV)	−0.754
F_{n2} (eV)	1.766
F_{n3} (eV)	−1.578
F_0 (eV)	−4.17
F_1 (eV)	0
F_2 (eV)	3.474
F_3 (eV)	2.288
F_e (eV)	−4.174

[31]. It is also in good agreement with the simulations using the analytic embedded atom method (AEAM), which yields $E_m = 0.19$ eV [32].

3 Results and discussion

3.1 kMC simulation results The performed kMC simulations investigate the kinetic shape of the islands. As a first step, deposition of Pt atoms was simulated, starting from a compact seed containing seven atoms. We have chosen the starting configuration with seven atoms due to the fact that these islands are already quite immovable (as pointed out by Müller et al. [33]). Even for such high deposition fluxes as 1000 ml/s, the kinetic shapes of the simulated islands are compact and triangle-like, as can be seen in Fig. 3.

The islands drawn with crosses are formed on HCP sites and the ones plotted with disks are formed on FCC sites. Formation of the stable HCP stacking islands is due to the high deposition flux (1000 ml/s) and low temperature (300 K). Under such conditions the islands created with more than five atoms on the HCP sites are stable in time, in spite of the well-known fact that the FCC stacking islands are energetically more favorable than the HCP ones. The triangular-shaped FCC and HCP stacking islands are both *B*-type islands. Due to the topological differences for the two different stackings, the direction of the HCP triangles is just the opposite of the FCC triangles.

As a second kMC study, in order to illustrate the stability of islands of different types, *A*- and *B*-type FCC triangular islands formed by 21 atoms are evolved at different temperatures, without depositing new atoms (deposition flux is zero). As can be seen in Fig. 4, for all the simulated temperatures (300, 400, 500, and 600 K) the *B*-type triangular islands will keep their orientation or become truncated *B*-type triangles. This clearly does not hold for the *A*-type islands. The islands that are initially of *A* type are distorted at lower temperatures and even inverted to *B*-type triangles at higher temperatures.

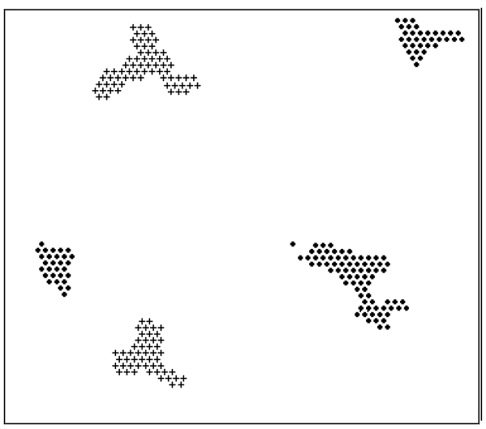

Figure 3 kMC simulation results for 1000 ml/s adatom deposition flux at 300 K after 227 kMC steps (corresponding to a real time of 4.3×10^{-5} s). The simulated system size is $64 \times 64 \times 4$, disks and crosses represent the atoms in the growing layer occupying FCC and HCP lattice sites, respectively.

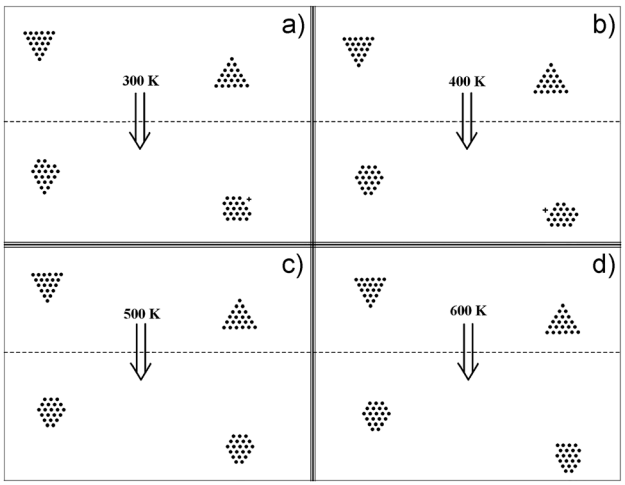

Figure 4 Time evolution of *A* (right) and *B* (left) type triangles without an external deposition flux. Each box indicates the initial (upper) and final (lower) configurations at different temperatures: (a) 488 Monte Carlo steps (corresponding to simulated time 7.6×10^{-2} s) at 300 K, (b) 490 Monte Carlo steps (6.9×10^{-3} s) at 400 K, (c) 149 Monte Carlo steps (1.4×10^{-3} s) at 500 K, and (d) 151 Monte Carlo steps (1.1×10^{-4} s) at 600 K.

3.2 Energy barrier calculations For a better understanding of both the triangular-shaped island formation phenomenon and the higher stability of the *B*-type triangular islands, in the following we will calculate the characteristic energy barriers for the relevant microscopical events.

First, the diffusion of Pt atoms on *A*- and *B*-type edges is studied. The energy barriers (or activation energies) for the jumps along the edges can be computed also from the statistics of the atom diffusion on these edges. On the top of a bulk FCC substrate a compact monolayer strip with three atomic rows is considered (Fig. 5). The diffusion of single Pt atoms can be now studied by kMC simulations on the two sides of this band. The bottom and top sides correspond to *A*- and *B*-type edges, respectively. The three atomic rows width of the band is enough, and is equivalent in our approach with an infinite-width step because the cutoff

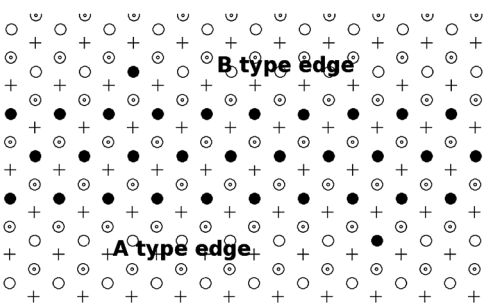

Figure 5 Diffusion of single atoms along *A*- and *B*-type edges of a 2D strip. Dotted circles represent the sites of the substrate, circles and crosses represent the FCC and HCP lattice sites of the growing layer, respectively. The filled circles are the FCC sites of the growing layer which are already occupied by the adatoms.

distance of the potential is set to three lattice constants. We recall here that the same cutoff distance was imposed also for all potential calculations on the bulk FCC lattice.

The diffusion coefficient (D) is calculated from the mean-square displacement of the atoms as a function of time. The common definition of D is

$$D = \frac{\left\langle (\Delta \mathbf{r}(t))^2 \right\rangle}{2d \times t}, \tag{8}$$

where $(\Delta \mathbf{r}(t))^2$ is the mean-square displacement of the atom in time t and d is the dimensionality of the motion. The ensemble average represented by the square brackets is an average computed from several independent realizations. In our case $d = 1$, the motions being restricted along the edges. D is computed by plotting $\left\langle (\Delta \mathbf{r}(t))^2 \right\rangle$ as a function of time and by determining the slope of the obtained linear dependence.

The diffusion coefficient is expected to exhibit the well-known Arrhenius-like behavior:

$$D = D_0 \exp\left(-\frac{E_m}{k_B T}\right). \tag{9}$$

In Eq. (9), D_0 is the pre-factor of the diffusion coefficient, E_m is a phenomenological activation energy (or migration energy) for the diffusing particle, k_B the Boltzmann constant, and T is the thermodynamic temperature of the system. D_0 and E_m can be calculated by plotting $\ln(D)$ as a function of $1/k_B T$. Results for single-atom diffusion on both the A- and B-type edges are presented on Fig. 6. These results prove the validity of the Arrhenius relation and indicate for the A-type edge $E_m = 0.36\,\text{eV}$ and $D_0 = 5.14 \times 10^{-3}\,\text{cm}^2/\text{s}$ and for the B-type edge $E_m = 0.6\,\text{eV}$ and $D_0 = 4.38 \times 10^{-3}\,\text{cm}^2/\text{s}$.

These activation energies are of course effective values, taking into account all possible type of jumps, namely the FCC–FCC, FCC–HCP, HCP–FCC, and HCP–HCP jumps. The results indicate a considerable difference for the single-atom diffusion coefficient on the two types of edges. They are also contradicting the early explanations [1] based solely on the differences in the diffusion coefficient values. Our results show that the atoms can diffuse more easily on the A-type edges; however, the stable island shape is the B-type triangle for all temperatures.

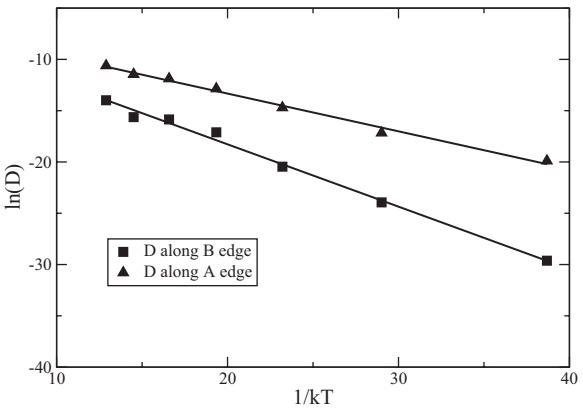

Figure 6 Arrhenius behavior for the diffusion of single atoms along A- and B-type edges.

Due to the fact that in our kMC approach the atoms can diffuse on both stackings, there are many topologically non-equivalent diffusion steps allowed. Going into more detail and studying separately these diffusion steps on both types of edges will help in a better understanding of the differences obtained for the diffusion coefficients. As an example, one can take the FCC–FCC type jumps along both edges and study the MEP of the individual diffusion steps on A- and B-type edges. We have chosen to discuss the FCC–FCC jumps, due to the fact that in all previously reported calculations only these diffusion jumps are considered and therefore this gives us a good ground for comparison.

For an FCC–FCC jump of an atom on the A-type edge the MEP contains an intermediate HCP site, and gives an energy barrier $E_{A_{2\to2}} = 0.372\,\text{eV}$. In contrast with this for an FCC–FCC jump on the B-type edge the MEP does not contain an intermediate site; therefore, the energy barrier is different: $E_{B_{2\to2}} = 0.589\,\text{eV}$. The topological differences for these FCC–FCC steps are clearly visible in Fig. 1. The anisotropy of edge diffusion for Al on Al(111) was also attributed to the topological (geometrical) differences of the A and B edges [34]. An explanation for the FCC–FCC jumps using HCP sites as intermediate sites for A-type edges was made by Brune [5], studying dendritic islands with triangular envelope.

With the presented NEB method it is possible to calculate the energy barriers for edge to corner and corner to edge jumps, denoted in the following as $E_{A_{1\to2}}$, $E_{A_{2\to1}}$, and $E_{B_{1\to2}}$, $E_{A_{2\to1}}$, respectively. These results (second column of Table 2) follow the expected $E_{1\to2} < E_{2\to2} < E_{2\to1}$ trend for both A and B edges, as was previously discussed by Wu et al.

Table 2 Energy barrier results for FCC–FCC jumps. Column 1 (GGA) summarizes the results of Feibelman [3]. Column 2 (NEB 19) presents our results with an unrestricted NEB and 19 replicas. Column 3 (NEB 19z) presents the results obtained with a NEB restricted perpendicularly on the surface and with 19 replicas. Column 4 (NEB 4) presents the results obtained by an unrestricted NEB with four replicas, and column 5 (NEB 4z) shows the results obtained with a NEB restricted perpendicularly on the surface and using four replicas.

	GGA	NEB 19	NEB 19z	NEB 4	NEB 4z
$E_{A_{1\to2}}$ (eV)	0.44	0.143	0.370	0.161	0.323
$E_{A_{2\to2}}$ (eV)	0.71	0.372	0.589	0.373	0.469
$E_{A_{2\to1}}$ (eV)	0.84	0.541	0.768	0.557	0.720
$E_{B_{1\to2}}$ (eV)	0.38	0.370	0.370	0.335	0.323
$E_{B_{2\to2}}$ (eV)	0.77	0.589	0.589	0.484	0.467
$E_{B_{2\to1}}$ (eV)	0.76	0.767	0.768	0.729	0.721

[4] who used Feibelman's generalized gradient approximation (GGA) calculations [3]. The results of GGA calculations are listed in the first column of Table 2. Our calculations with 19 NEB nodes show that for all three cases ($1 \rightarrow 2$, $2 \rightarrow 2$, and $2 \rightarrow 1$), the energies on the *A*-type edge are smaller than the corresponding energies for the *B*-type edge (second column of Table 2). We recall here that all the calculated energy values are for FCC–FCC jumps; therefore, the energies of $2 \rightarrow 2$ jumps will differ slightly from the effective energies calculated from the diffusion along the edges.

From the results presented in Table 2, one can conclude that atoms on *A*-type edges can diffuse more easily than atoms on *B*-type edges and this holds not only along the edges, but also for jumps to and from the corners.

The energy barriers calculated by Feibelman [3] differ (sometimes considerably) from those calculated by us. In almost all cases our calculations underestimate the GGA results. This is somehow expected for a semi-empirical approach next to an *ab initio* calculation, which ought to be much more precise. The differences might also come from the fact that the gEAM potentials are more appropriate for bulk atoms than surface ones. This can be also seen in our results for the free diffusion of a Pt atom on a Pt(111) surface, where an error of order 20% is obtained for the energy barrier value calculated with gEAM and NEB relative to the value obtained in experiments. The larger deviations observable for jumps on *A*-type edges might also be a consequence of the differences between the performed NEB calculations.

In our kMC method we have used 19 replicas (NEB nodes) of the system, while in the GGA calculations only four replicas were used. In order to investigate whether the large differences in Table 2 are due to the implementation of the NEB method, we have made some further studies.

First, we relaxed the NEB using the gEAM potential with 19 replicas of the system, but restricted the band only in a perpendicular direction to the surface. Under such restrictions the energies are already closer to the GGA calculations (third column of Table 2). In this restricted case the MEP for FCC–FCC jumps on *A*-type edges will not contain intermediate HCP sites, because the band will not flare out in sideways directions and as a result of this the energy barriers are the same for jumps along *A*- and *B*-type edges. We suspect thus that in the work of Feibelman [3] such restrictions were also imposed.

Secondly, if the calculations are taken with only four NEB nodes, the energy barriers calculated from a spline fit can be quite far from the real values. This is illustrated in Fig. 7 for $A_{2\rightarrow 2}$ FCC–FCC jumps. For the sake of comparison we also show that by using 19 nodes, the energy plot of the nodes is much more smooth. The local minimum for the unrestrictedly relaxed band indicates the presence of the intermediate HCP site. One can also observe that the results obtained by us with only four NEB nodes are now much closer to the GGA results. Taking into account the difference in how the NEB method was implemented in the present study and in the study of Feibelman [3], we suspect that the larger deviations in the obtained energy barriers are not due to the interatomic potential values used, but due to the NEB calculations.

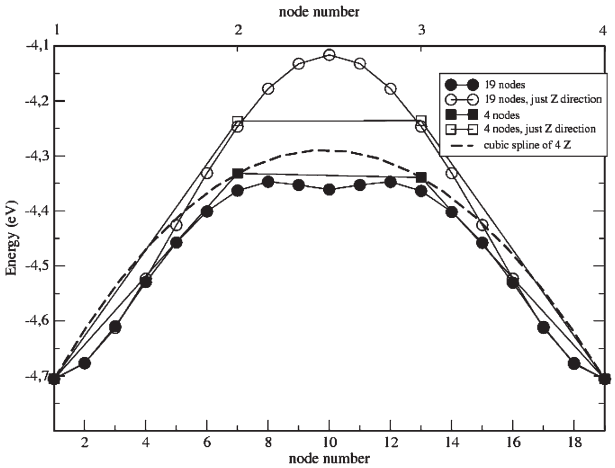

Figure 7 NEB node energies for bands containing 19 and four nodes, for both unrestricted and perpendicularly restricted (*z*-direction) relaxations of $A_{2\rightarrow 2}$ FCC–FCC jumps.

The kink-formation and kink-breaking phenomenon (Fig. 8) is another elementary process in step advancement and therefore can be an important process in triangle-shape formation. The energy barriers calculated for kink-formation and kink-breaking events are listed in Table 3.

Summarizing now the above-discussed results, one can list the following statements that could help in explaining the creation of the *B*-type triangular islands:

(1) The diffusion of atoms on *A*-type edges is easier than on *B*-type edges.
(2) The kink formation is easier on *A*-type edges than on *B*-type ones.

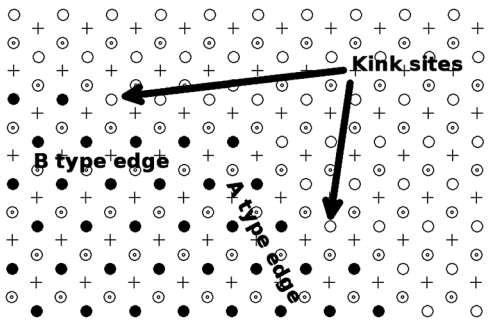

Figure 8 Kink sites on *A*- and *B*-type edges.

Table 3 Calculation results.

	kink-formation energy	kink-breaking energy
on *A* edge	0.281 eV	0.624 eV
on *B* edge	0.469 eV	0.830 eV

(3) On *A*-type edges the kink-breaking energy is high enough relative to the kink-formation energy in order to allow the step advancement on these edges.
(4) The $E_{A_{1\to 2}} < E_{B_{1\to 2}}$ relation is favorable for *A*-step advancement, because the probability for a corner atom to choose the *A* edge is higher than the probability for choosing the *B*-type edge.

Items 1 and 4 alone do not suggest the growth of *B*-type triangles. These effects would favor a more rapid growth of the *B*-type edges and ultimately the formation of *A*-type triangles. The facts summarized under items 3 and 4 are however responsible for the quicker advancement of the *A*-type edges leading to the formation of *B*-type triangular compact islands. Seemingly these later effects are the stronger ones, and will favor the growth of *B*-type triangles.

4 Conclusions The aim of the present work was to reconsider the formation of *B*-type triangular-shaped Pt adatom islands on a Pt(111) surface by using a kMC simulation method, which has proven its applicability in a recent study concerning the adatom island diffusion [19]. Computer simulations and calculations were done using the gEAM potential, taking into account all possible FCC–FCC, FCC–HCP, HCP–FCC, and HCP–HCP jumps on the Pt(111) surface. The energy barriers for the jumps were calculated with the NEB method using 19 replicas of the system.

By studying individually and collectively the diffusion of Pt atoms along the island edges, a more complete picture about the formation of triangular islands and their stability in time was drawn. The obtained results indicate a higher diffusion speed of atoms along *A*-type island edges. Also, the jump rates from edge to corner and corner to edge are higher for *A*-type edges compared to *B*-type ones. These results alone do not explain the better stability of the *B*-type islands, but, on the contrary, taking into account the earlier explanations [1, 2, 4, 7, 16], these results suggest a more stable *A*-type triangular island.

Studying the energies necessary for kink formation and kink breaking reveals however that the atoms will assemble with a higher probability on *A*-type edges, leading to a higher advancement speed of the *A*-type steps. The higher jump probability from the corner sites to *A*-type edges leads also to a quicker advancement of *A*-type edges and ultimately to the formation of *B*-type triangular-shaped islands. We hope that the present study will help in a better understanding of the formation of triangular-shaped Pt islands on a Pt(111) surface.

Acknowledgements This work was supported by grant PN II/PCCE 312/2008 on Complex Ideas.

References

[1] Th. Michely, M. Hohage, M. Bott, and G. Comsa, Phys. Rev. Lett. **70**, 3943 (1993).
[2] M. Kalff, G. Comsa, and Th. Michely, Phys. Rev. Lett. **81**, 1255 (1998).
[3] P. Feibelman, Phys. Rev. B **60**, 4972 (1999).
[4] J. Wu, E. G. Wang, K. Varga, B. G. Liu, S. T. Pantelides, and Z. Zhang, Phys. Rev. Lett. **89**, 146103-1 (2002).
[5] H. Brune, Surf. Sci. Rep. **31**, 121 (1998).
[6] H. Brune, G. S. Bales, J. Jacobsen, C. Boragno, and K. Kern, Phys. Rev. B **60**, 5991 (1999).
[7] S. Ovesson, A. Bogicevic, and B. I. Lundqvist, Phys. Rev. Lett. **83**, 2608 (1999).
[8] Th. Michely and J. Krug, Islands, Mounds and Atoms (Springer, Berlin, 2004,).
[9] J. W. Evans, P. A. Thiel, and M. C. Bartelt, Surf. Sci. Rep. **61**, 1 (2006).
[10] P. Zhang, Y. Xie, X. Ning, and J. Zhuang, Nanotechnology **19**, 255704 (2008).
[11] C. Yin, X.-J. Ning, J. Zhuang, Y.-Q. Xie, X.-F. Gong, X.-X. Ye, C. Ming, and Y.-F. Jin, Appl. Phys. Lett. **94**, 183107 (2009).
[12] G. Cao, Nanostructures and Nanomaterials, Synthesis, Properties and Applications (Imperial College Press, London, 2004).
[13] D. W. Basset and P. R. Webber, Surf. Sci. **70**, 520 (1978).
[14] T.-Y. Fu, Y.-R. Tzeng, and T. T. Tsong, Phys. Rev. B **54**, 5932 (1996).
[15] S. Liu, Z. Zhang, G. Comsa, and H. Metiu, Phys. Rev. Lett. **71**, 2967 (1993).
[16] J. Jacobsen, K. W. Jacobsen, and J. K. Norskov, Surf. Sci. **359**, 37 (1996).
[17] R. Deák, Z. Néda, and P. B. Barna, J. Optoelectron. Adv. Mater. **10**, 2445 (2008).
[18] A. F. Voter, Phys. Rev. B **34**, 6819 (1986).
[19] R. Deák, Z. Néda, and P. B. Barna, Commun. Comput. Phys. **10**, 920 (2011).
[20] R. Deák, Z. Néda, and P. B. Barna, Commun. Comput. Phys. **3**, 822 (2008).
[21] M. Kotrla, J. Krug, and P. Smilauer, Phys. Rev. B **62**, 2889 (2000).
[22] A. B. Bortz, M. H. Kalos, and J. L. Lebowitz, J. Comput. Phys. **17**, 10 (1975).
[23] A. F. Voter and J. D. Doll, J. Chem. Phys. **80**, 5832 (1984).
[24] G. Mills and H. Jonsson, Phys. Rev. Lett. **72**, 1124 (2001).
[25] G. Henkelman and H. Jonsson, J. Chem. Phys. **113**, 9978 (2000).
[26] G. Henkelman and H. Jonsson, J. Chem. Phys. **111**, 7010 (1999).
[27] H. N. G. Wadley, X. Zhou, R. A. Johnson, and M. Neurock, Prog. Mater. Sci. **46**, 329 (2001).
[28] X. W. Zhou, H. N. G. Wadley, R. A. Johnson, D. J. Larson, N. Tabat, A. Cerezo, A. K. Petford-Long, G. D. W. Smith, P. H. Clifton, R. L. Martens, and T. F. Kelly, Acta Mater. **49**, 4005 (2001).
[29] P.-H. Huang, T.-H. Fang, and C.-S. Chou, Curr. Appl. Phys. **11**, 878 (2011).
[30] D. Marx and J. Hutter, in: Proc. Modern Methods and Algorithms of Quantum Chemistry, 2nd edn. (NIC Ser.) (John von Neumann Institute for Computing, Julich, 2000).
[31] K. Kyuno and G. Ehrlich, Surf. Sci. **437**, 29 (1999).
[32] J. Yang, W. Hu, and M. Xu, Appl. Surf. Sci. **255**, 1736 (2008).
[33] M. Müller, K. Albe, C. Busse, A. Thoma, and Th. Michely, Phys. Rev. B **71**, 075407-1 (2005).
[34] A. Bogicevic, J. Strömquist, and B. I. Lundqvist, Phys. Rev. Lett. **81**, 639 (1998).

